A Reduced-Order-Model-Based Motion Selection Strategy in a Leg-Wheel Transformable Robot

Ting-Hao Wang and Pei-Chun Lin ⬛, *Senior Member, IEEE*

Abstract—**This article reports on a model-based methodology for a leg-wheel transformable robot to autonomously determine the use of the wheeled or legged mode based on environmental RGB-Depth information. A concentric and reduced-order dual-leg-wheel model was developed to explore the dynamic interactions between the leg-wheel and terrain. The simulation results revealed that terrain height variation acts as the key factor in determining the model's terrain negotiability; therefore, it was utilized as the decision index for leg-wheel motion selection. To facilitate real-time motion selection on the empirical robot, a two-step selection strategy utilizing RGB-Depth information was proposed. The first step utilized RGB images to classify seven types of terrain. If the classified terrain was potentially rough, the second step utilized depth images to compute the terrain height variation, which was then compared to the index derived by the dual-leg-wheel model to select the final operation mode. The strategy was implemented on a leg-wheel transformable robot and experimentally validated on various types of terrain. The results confirm that the robot's behavior closely resembled the model's prediction, and using the proposed strategy to select leg-wheel motion in the robot yielded the most energy efficient locomotion.**

Index Terms—**Hybrid robot, legged, motion decision, RGB-Depth, terrain classification, transformable robot, wheeled.**

I. INTRODUCTION

AUTONOMOUS mobility can be regarded as one of the most important capabilities of mobile robots. This capability relies on the cyclic and periodic process of sensing, decision, and motion generation, so the robot can instantly and robustly make an adequate response to environmental conditions. Research associated with wheeled mobile robots usually focuses on localization and navigation problems. In contrast, a legged robot focuses on the stride-level or short-distance legged mobility problem.

In addition to ordinary wheeled or legged mobile robots [1], hybrid leg-wheel robots were designed to enhance mobility. Besides, mounting wheels on the end of articulated legs [2] or mounting additional active structures onto wheels as legs [3], [4], some works have focused on designing transformable mechanisms using extensible wheel rims to form the legs [5]–[8], or to transform between wheel, leg and track [9]. Previously, we developed a leg-wheel transformable robot *Quattroped*
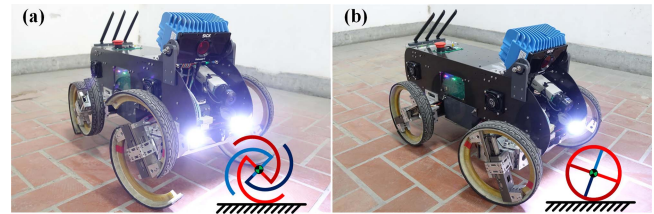
Fig. 1. Photos of the leg-wheel transformable robot *TurboQuad* and the corresponding simplified dual-leg-wheel models. (a) In legged mode. (b) In wheeled mode.

[10], which utilized the same set mechatronic system to drive both leg and wheel modes. Later, successor *TurboQuad* [11] shown in Fig. 1 further enabled *in situ* smooth gait/mode transition and leg-wheel transformation during locomotion. The robot was capable of performing SLIP-like running behavior as well [12] based on "template and anchor" methodology [13], [14]. Along with the development of hybrid robots, we found that the reported research mainly focused on innovative mechanism design for hybrid locomotion. Some research focused on gait development by optimizing forward speed and energy consumption using full body dynamic simulation [15], and some analyzed the deduced model to calculate the optimal joint torques of the feet [16]. In contrast, the strategy at the decision level, which determines adequate use of behaviors (i.e., wheeled, legged, or others), was rarely discussed in the community. A simulation-based long-distance navigation planner relying on given terrain geometry has been utilized in the leg-wheel hybrid robot LEON [7]. However, to the best of our knowledge, no published works have addressed decision-level strategies for leg-wheel hybrid robots to determine the use of legged or wheeled behavior based on their mechanism characteristics and limited, short-distance, and real-time environmental information.

Instead of searching for optimized motion strategies for the robot to use on each type of terrain based on a delicate sensing system and a motion controller, we were interested in exploring whether there exists a basic rule for the robot to select the optimal operation mode based on a simple sensing and selection rule that is straightforward and sufficiently general for implementation in other relevant applications. Furthermore, instead of conducting heuristic experimental tests on the robot to find the rule, we preferred tackling the problem using reduced-order models because these models were easier to construct, analyze, and apply to find motion tendencies than full-body models. We evaluated motion performance using different formations of the leg-wheel robot in a simplified but representative simulation environment and identified the most effective behavior selection strategy to achieve autonomous switching with improved motion efficiency on our robot. Thus, the novelty and contribution of this article lies not only in the simple strategy yielded but also the proposed methodology, which utilizes reduced-order model-induced behavior to explore and coordinate the
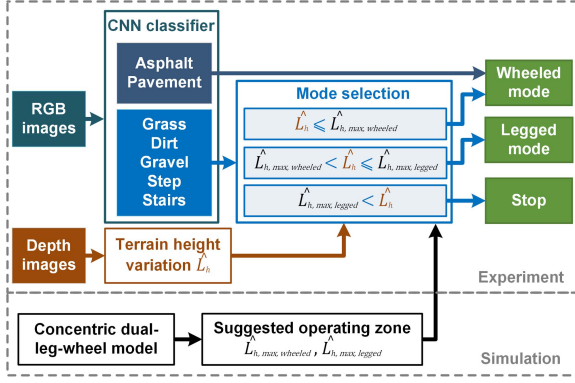
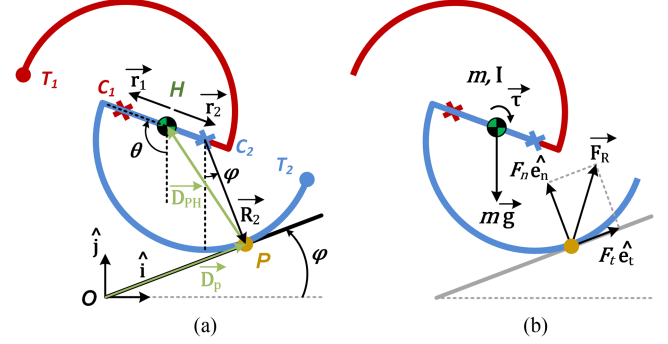Fig. 2. Decision process of the leg-wheel motion selection strategy.

Fig. 3. Single leg-wheel model. (a) Geometric notations. (b) Mechanical parameters and the free body diagram.

Fig. 4. Three contact scenarios of the leg-wheel model. (a) Rolling contact. (b) Point contact. (c) Edge contact.

existing sensing technique for autonomous leg-wheel motion selection of the leg-wheel hybrid robot.

The proposed strategy is shown in Fig. 2, which focuses on two major tasks. First, we develop a reduced-order model and analyze the complex leg-wheel dynamic interactions with the ground, and the analysis reveals that a simple but representative index, level height $\hat{L}_h$, governs the performance. We determine the most suitable operating upper bounds $\hat{L}_{h,\max}$ for the legged and wheeled mode to form the suggested operating zone. Then, we formulate a leg-wheel selection strategy that relies on a perception system to gather essential environmental RGB-Depth data for the real-time decision process. The RGB images are utilized to classify the terrain into one of the seven categories using an off-the-shelf convolution neural network (CNN) technique. If the predicted terrain is generally flat, the wheeled mode is directly utilized. If the predict terrain is potentially rough, the approximated height variation $\hat{L}_h$ is computed using a depth sensor in real time. Then, the value $\hat{L}_h$ is compared to $\hat{L}_{h,\max}$ of the suggested operating zone (SOZ) to select the most appropriate behavior, legged, or wheeled.

The rest of the article is organized as follows. Section II described the development of the concentric dual-leg-wheel model, and Section III reports on the leg-wheel selection strategy. Section IV describes the experimental results, and finally, Section V concludes this article.

II. CONCENTRIC DUAL-LEG-WHEEL MODEL

Due to the complexity involved in developing a full-body model and the possibility of overfitting it to a specific platform without generality, the simplified concentric dual-leg-wheel model was developed to capture the essential motion dynamics of the robot negotiating in a real environment and to extract the variable that governs the motion performance.

A. Formulation of the Model

As shown in Fig. 1, the concentric dual-leg-wheel model is composed of two concentric leg-wheels at the hip joint. Each leg-wheel, as depicted in Fig. 3, closely resembles the morphology of the robot's leg-wheel and is composed of two half-circular legs with radius R, centers $C_{i,\ i=1,2}$, and feet $T_{i,\ i=1,2}$, respectively. The symbol $\vec{r_i}$ refers to the vector from hip joint H to the center of half-circle C_i. The leg-wheel can rotate and translate with respect to H, which is also the center of mass (COM) of the model; thus, it is capable of mimicking the extracting and retracting motion of an articulated leg [11]. Because the two half-circular legs move synchronously, the leg-wheel has two degrees of freedom in its movement, along with the polar coordinates originating at H, (θ, r), $r = |\vec{r_1}| = |\vec{r_2}|$. When the centers $C_{i,\ i=1,2}$
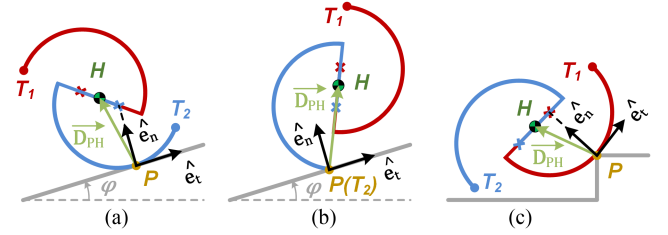
coincide with H, two half-circular legs form a circle and turn into a wheel (i.e., $r = 0$), and the model operates in wheeled mode, as shown in Fig. 1(b). Otherwise, the leg-wheel operates in legged mode, as shown in Fig. 1(a).

The dynamics of the leg-wheel were formulated using the Newtonian method. First, the position vector of the COM, $\overrightarrow{D_H}$, was derived based on the geometric configuration of the leg-wheel with respect to the terrain. As shown in Fig. 3(a),

$$\overrightarrow{D_H} = \overrightarrow{D_P} + \overrightarrow{D_{PH}} = \overrightarrow{D_P} + \left(-\overrightarrow{R_i} - \overrightarrow{r_i} \right) \tag{1}$$

with $\overrightarrow{r_i} = (-1)^i \, r(\sin\theta\hat{i} + \cos\theta\hat{j})$

$$\overrightarrow{R_i} = \begin{cases} R\left(\sin\varphi\hat{i} - \cos\varphi\hat{j}\right), & \text{rolling and edge contact} \\ (-1)^i R\left(\sin\theta\hat{i} + \cos\theta\hat{j}\right), & \text{point contact} \end{cases}$$

$\overrightarrow{R}_{i,\ i=1,2}$ refers to the vector from C_i to P, which has two formulations based on the leg-wheel's three contact scenarios shown in Fig. 4. Therefore, $\overrightarrow{D_{PH}}$ and $\overrightarrow{D_H}$, which are later utilized in the equations of motion (EOM), can be derived as follows.

Rolling and edge contact:

$$\overrightarrow{D_{PH}} = \left[-R\sin\varphi - (-1)^i r\sin\theta \right]\hat{i} + \left[R\cos\varphi - (-1)^i r\cos\theta \right]\hat{j} \tag{2}$$

$$\overrightarrow{\ddot{D}_H} = \left\{ \ddot{\theta}\left[-R\cos\varphi - (-1)^i r\cos\theta \right] + \dot{\theta}^2\left[R\sin\varphi + (-1)^i r\sin\theta \right] \right\}\hat{i} + \left\{ \ddot{\theta}\left[-R\sin\varphi + (-1)^i r\sin\theta \right] + \dot{\theta}^2\left[R\cos\varphi + (-1)^i r\cos\theta \right] \right\}\hat{j} \tag{3}$$

Point contact:

$$\overrightarrow{D_{PH}} = -(-1)^i \, (R + r)\left(\sin\theta\hat{i} + \cos\theta\hat{j} \right) \tag{4}$$

$$\overset{\cdots}{\overrightarrow{D_H}} = -(-1)^i \ (R+r) \left[\left(\ddot{\theta} \cos\theta - \dot{\theta}^2 \sin\theta \right) \right.$$
$$\left. \hat{i} - \left(\ddot{\theta}\sin\theta + \dot{\theta}^2 \cos\theta \right) \hat{j} \right] \tag{5}$$

In derivation of $\overset{\cdots}{\overrightarrow{D_H}}$, $\overrightarrow{D_P}$ was assumed constant because of its infinitesimal movement. Next, the EOM of the leg-wheel were derived based on the free body diagram, as shown in Fig. 3(b). The model has mass m at the COM and inertia $I(r)$ with respect to the COM, a function of r. The forces include the leg-wheel's driving torque τ, gravitational force $m\vec{g}$, and ground reaction force $\overrightarrow{F_R} = F_t\,\hat{e}_t + F_n\hat{e}_n$ in natural coordinates, where F_t and F_n correspond to the friction force and normal force of the terrain, respectively. Depending on contact slippage between the leg-wheel and terrain, the friction force F_t has two possible values according to the Coulomb friction law:

$$F_t = \begin{cases} F_t, \ if \ F_t \le \mu_s F_n \ no-\text{slippage} \\ \mu_k F_n, \ if \ F_t > \mu_s F_n \ \text{slippage} \end{cases} \tag{6}$$

Note that the directions of $\hat{e}_t$ and $\hat{e}_n$ vary depending on the contact scenario, as shown in Fig. 4. Finally, the translational and rotational EOMs of the leg-wheel were formulated using Newton's law of motion:

$$\begin{cases} m \overset{\cdots}{\overrightarrow{D_H}} = m\vec{g} + \overrightarrow{F_R} \\ I \overset{\cdots}{\vec{\Theta}} = \vec{\tau} - \overrightarrow{F_R} \times \overrightarrow{D_{PH}} - C_d \dot{\vec{\Theta}} \end{cases} \tag{7}$$

Where $\vec{\Theta} = [\,0 \ 0 \ \theta\,]$ and C_d denotes the resultant damping coefficient that remedies the energy loss in the model.

The motion of the dual-leg-wheel model moving on a terrain was computed recursively based on the EOMs of two sets of leg-wheels using MATLAB, as shown in (7). The motion was computed in small time increments because the contact dynamics varied, such as the contact leg, contact scenario, contact point, and leg slipping/nonslipping condition. Fig. 5 shows a flowchart of the algorithm, which includes three checks/adjustments from different aspects at each time stamp:

1) Contact Condition Check: The existence of the contact condition between the dual-leg-wheel model and the terrain is checked. If not, the model falls using the ballistic model. If yes, the algorithm enters the next check.

2) Geometric Adjustment: The differential motion of the dual-leg-wheel model is computed based on the final body states of the model at the previous time stamp. If the model has geometric confliction with the ground, as Fig. 5(b) shows (i.e., the model's leg-wheel penetrates into the ground), the model is incrementally lifted till the contour to be exactly tangent to the ground at point(s) P. These point(s) are regarded as the potential contact point(s). The computation details are described as follows. The penetrated section $Q_1 Q_2$ is computed, which is projection of the leg-wheel on the ground with respect to the leg-wheel's center C. Then, the new contact point P, which is along with $Q_1 Q_2$ and has the shortest distance to C, is computed. The $\overrightarrow{D_{CP}}$ vector is then extended to intersect with the leg-wheel at point A. Finally, the leg-wheel is lifted along with $\overrightarrow{D_{AP}}$ until the leg-wheel coincides with P. If more than one section of the leg-wheel penetrates the ground, the lifting direction and magnitude is the union of all lifting vectors, and instantaneous center of rotation is set to be the forefront one.

3) Kinetics Adjustment: Based on the adjusted final states of the model at the previous time stamp, as well as the given leg-wheel motion trajectories versus time, $(\boldsymbol{\theta}(t), \boldsymbol{r}(t))$, the dynamic motion of the dual-leg-wheel model at this specific time stamp was computed using (7). The EOMs yield the required $\overrightarrow{F_R}$ for motion without slippage. Then, the assumed no-slippage condition was checked using a friction cone [17].
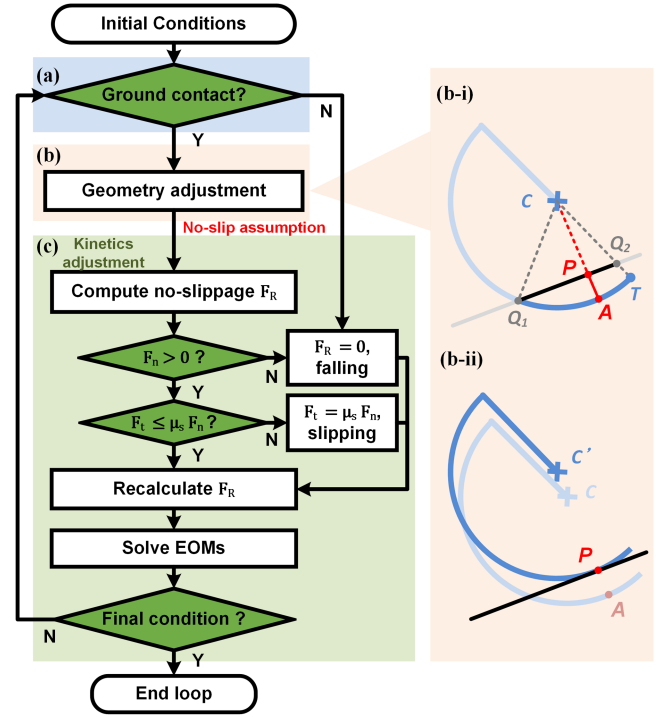

Fig. 5. Flow chart of the computational simulation of the dual-leg-wheel model. The three blocks in different colors refer to the three checks/adjustments. (a) Contact condition check. (b) Geometry adjustment. (c) Kinetics adjustment.

If the assumption was not satisfied, the modified $\overrightarrow{F_R}$, which utilized kinetic friction, as shown in (6), was computed. Then, the modified $\overrightarrow{F_R}$ was imported into (7) to recompute the COM state $\overrightarrow{D_H}$, which represents the correct body state of the model at this specific time stamp.

These three checks/adjustments are computed at every time stamp in the sequence. Finally, the motion of the dual-leg-wheel model can be derived by integrating these differential motions.

Three performance indices were defined and utilized to evaluate the performance of the model that negotiated rough terrain using the wheeled or legged mode. The indices included the averaged forward velocity of the COM $v_{x,\text{avg}}$ (i.e., the ability to cross through the landscape), the averaged work per COM traveled forward distance w_{avg} (i.e., the energy cost per unit forward distance), and the sum of the hip oscillation along a vertical direction per traveled distance δ_{avg} (i.e., the index for motion smoothness) between time stamps $[t_i, t_f]$:

$$v_{x,\text{avg}} = \frac{d_{x,t_f} - d_{x,t_i}}{t_f - t_i}, \ w_{\text{avg}}$$
$$= \frac{\sum_{t_i}^{t_f} \left| \dot{\theta}(t)\,\tau(t) \right|}{d_{x,t_f} - d_{x,t_i}}, \ \delta_{\text{avg}} = \frac{\sum_{t_i}^{t_f} |d_{y,t+\Delta t} - d_{y,t}|}{d_{x,t_f} - d_{x,t_i}} \tag{8}$$

Note that the average of instantaneous speeds throughout the trajectory is equal to the simple average shown in (8). When the w_{avg} is normalized by weight, the index is equivalent to the specific resistance [18]. These indices directly indicate the negotiability, energy consumption, and motion smoothness of the model, respectively. The forward distance between stamps $[t_i, t_f]$ was computed and summed. When slippage exists, the kinetic friction is utilized in equations of motion. In this case, the forward distance would drastically decrease. If the model
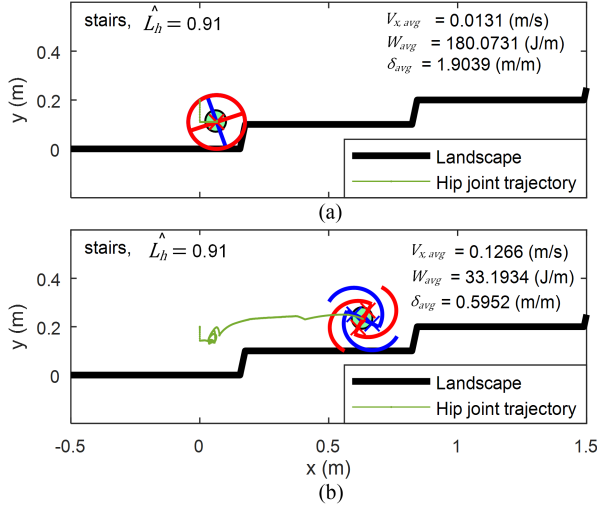
Fig. 6. COM trajectories and the performance indices of the dual-leg-wheel model when negotiating the stair with $\hat{L}_h = 0.91$, $(\mu_s, \mu_k) = (1.0, 0.9)$, $v_f = 0.2$ (m/s) using (a) wheeled and (b) legged mode.

failed to pass, then $v_{x,\text{avg}}$ tended to decrease to zero, whereas w_{avg} and δ_{avg} increased.

B. Simulation Results

Many uneven terrains exist in the environment; among them, steps can be regarded as the basic form. For example, stairs are the sequential composition of steps and a tree root can be regarded as the curvy bars with height and lateral shape variations. The model's ascent ability requires stronger attention than descent ability since the gravity force can assist the model motion in the latter case. Unlike a wheel, which has uniform motion behavior to negotiate steps, legs exhibit a wide range of terrain negotiating behaviors, depending on the initial relative configuration between the leg and the step. Therefore, stairs were chosen as the scenario for simulation. In practical implementation, it would be difficult to include the stair length in the decision process due to the real-time sensing constraint (i.e., out of view). Therefore, the level height of the stair was varied but not the stair length.

Three factors (i.e., the normalized level height $\hat{L}_h \equiv L_h/R$, surface friction of the stairs (μ), and motion pattern of the dual-leg-wheel model) were varied in simulations to evaluate the model's ability to navigate stairs in both wheeled and legged modes. For simplicity, the relation between static and kinetic friction coefficients was assumed to be $\mu_k = \mu_s - 0.1$. Trotting was utilized as the dual-leg-wheel driving pattern $(\theta(t), r(t))$ with nominal forward speed $v_f = 0.2$ and 0.4 (m/s), which were computed based on the assumption of the leg-wheel rolling without slippage on flat ground. The detailed computation of nonlinear forward and inverse kinematics between the leg-wheel states $(\theta(t), r(t))$ and the COM states can be found in [11].

Fig. 6 shows examples of the snapshots of the COM trajectories of the concentric dual-leg-wheel model in the legged and the wheeled modes, and the complete videos can be found in the supplementary material. The result reveals the advantage of using the legged mode over the wheeled mode, where the latter could not climb up the stairs. In this scenario, the former has better performance in all indices (i.e., higher $v_{x,\text{avg}}$ and lower w_{avg} and δ_{avg}) than the latter.

Fig. 7 shows the summarized simulation results of the model negotiating stairs with different $\hat{L}_h$ and μ settings. The initial configuration of the leg-wheel of the model (i.e., θ_{initial}) was varied as well to
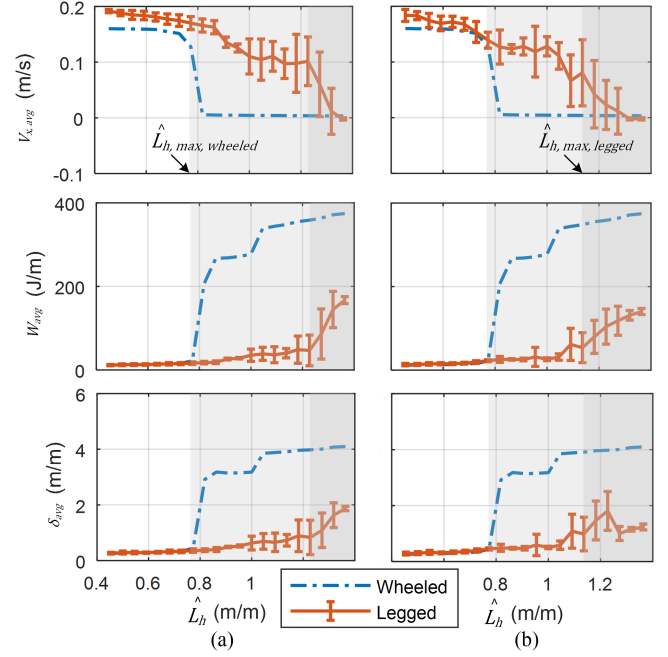

Fig. 7. Three performance indices of the dual-leg-wheel model in wheeled and legged modes versus $\hat{L}_h$ with $v_f = 0.2$ (m/s) and under two μ settings: (a) $(\mu_s, \mu_k) = (1.0, 0.9)$ and (b) $(\mu_s, \mu_k) = (0.6, 0.5)$. The figure reveals that $\hat{L}_{h,\text{max,wheeled}}$ can serve as the index for the model to select legged mode or wheeled mode for better traversability, efficiency, and stability. The exploring precision for $\hat{L}_h$ was set at 0.5% of the incremental change when compared to the radius of the wheel.

cover a wide range of possible contact conditions, and the results are summarized in a statistical manner. Because the model in the wheeled mode did not have configuration difference under varied θ_{initial}, the results were identical with zero standard deviation. In contrast, the model in the legged mode with different initial configurations had distinct performance. A new index *the critical operating height* $\hat{L}_{h,\text{max}}$ was defined to identify the maximum $\hat{L}_h$ the model could negotiate. When the model negotiated the obstacle with a height higher than $\hat{L}_{h,\text{max}}$, the $V_{x,\text{avg}}$ of the model dramatically approached zero, and W_{avg} and δ_{avg} increased. Fig. 7 reveals that $\hat{L}_{h,\text{max}}$ of the model in the legged mode, $\hat{L}_{h,\text{max,legged}}$, is higher than that with wheeled mode, $\hat{L}_{h,\text{max,wheeled}}$, in both surface friction status. This indicates the model in the legged mode has better traversability on negotiating barriers when $\hat{L}_{h,\text{max,wheeled}} < \hat{L}_h \leq \hat{L}_{h,\text{max,legged}}$. In contrast, when $\hat{L}_h \leq \hat{L}_{h,\text{max,wheeled}}$, the model in the wheeled mode has better performance with a lower W_{avg} and δ_{avg}. Thus, the figure reveals that $\hat{L}_h$ governed the outcomes of the three indices. Besides, $\hat{L}_{h,\text{max,wheeled}}$ was served as a critical index to determine the use of the wheeled or legged mode. When the height of the obstacle of $\hat{L}_h$ is no greater than $\hat{L}_{h,\text{max,wheeled}}$, the model utilizes the wheeled mode to achieve higher efficiency and stability. Otherwise, the model uses the legged mode for better traversability.

Fig. 8 shows $\hat{L}_{h,\text{max,wheeled}}$ and $\hat{L}_{h,\text{max,legged}}$ on the terrain with more friction settings, and this figure reveals the SOZ of the leg-wheel. Parameterized by outcomes of three defined indices shown in (8), the simulation result reveals that the step height governs the negotiability of the robot much more than the friction and forward speed do. The $\hat{L}_{h,\text{max,wheeled}}$ maintains similar value between $\mu_s = 0.6 - 0.8$ at both speeds, and at high speed, it increases no more than 18%, while μ_s increases to 1.0. Because variation of $\hat{L}_{h,\text{max,wheeled}}$ is not significant
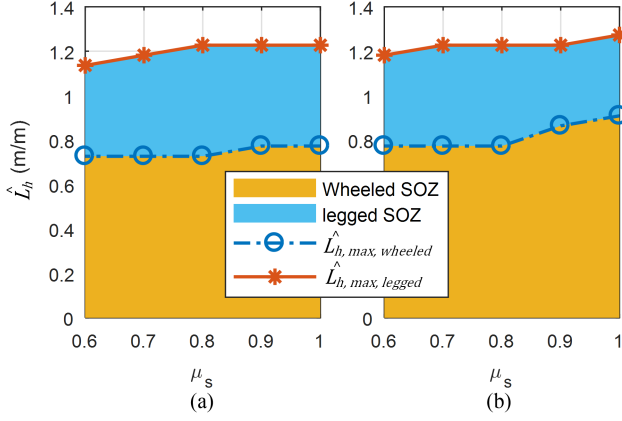
Fig. 8. SOZ of the leg-wheel model at forward speeds (a) $v_f = 0.2$ (m/s) and (b) $v_f = 0.4$ (m/s). The operating points lay on the line of $\hat{L}_{h,\max,\text{wheeled}}$ are the suggested transition conditions between wheeled and legged mode.
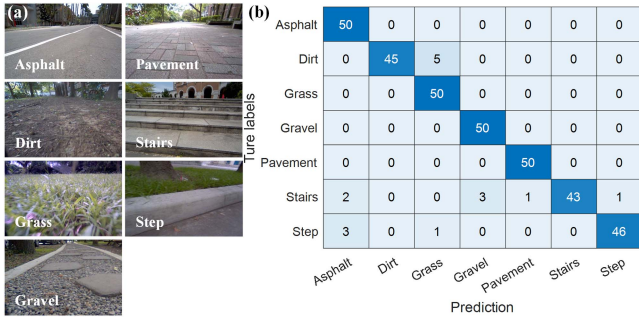

Fig. 9. (a) Example of an image dataset including seven categories. (b) Confusion matrix that validates the performance of the terrain classification with 95.43% accuracy.

and in situ μ_s measurement is challenging, $\hat{L}_{h,\max,\text{wheeled}} = 0.75$ was chosen to grant the terrain negotiability of the model in the wheeled mode. Based on a similar concept, $\hat{L}_{h,\max,\text{legged}} = 1.15$ was chosen for the negotiating limitation for the model in the legged mode. To apply the suggestions from the results of the model to the empirical robot, the height variation $\hat{L}_h$ of the terrain should be measured on board and in real time.

III. LEG-WHEEL MOTION SELECTION STRATEGY

The proposed leg-wheel motion selection strategy for the robot to determine the usage of the wheeled or legged mode for terrain negotiation in real time includes two steps. The first step utilizes RGB images to classify the terrain into seven types: asphalt, pavement, grass, dirt, gravel, steps, and stairs. For empirically flat terrain, such as asphalt or pavement, the wheeled mode is directly utilized, as shown in Fig. 2. For potentially rough terrain, the second step is processed. It utilizes depth images to compute the required height variation $\hat{L}_h$. The measured height $\hat{L}_h$ was then compared to the SOZ derived by the model to select the final operation mode.

In the first-step processing, the CNN modified from the off-the-shelf AlexNet [19] was utilized for terrain classification. In each category, at least 1000 images under manifold shooting conditions were collected at both daytime and nighttime for supervised learning, including illumination changes or interferences from small portions of outliers inside the images. A few examples are shown in Fig. 9(a).
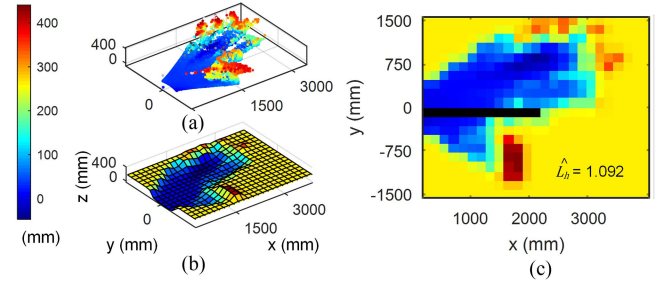

Fig. 10. Processing of depth information. (a) Depth point cloud represented in the robot frame. The x-axis and z-axis represent the forward and vertical direction, respectively. The color represents data in different heights (z). (b) Grid elevation map. (c) Top view of the grid map, where the black straight line ahead the robot represents ROI.

As shown in Fig. 10, the second-step processing involves several tasks related to the elevation map [20]. First, the raw two-dimensional distance matrix measured from the depth sensor is transformed into the robot's coordinates after being filtered with the intensity and confidence signal, as shown in Fig. 10(a). Then, the exploring space is divided into grids with side lengths of 200 mm along the horizontal plane, and the mean height of each grid is computed, as shown in Fig. 10(b). Grids without data points due to occlusion or a far distance were assigned a relatively high height. Gaussian blur was also applied to the elevation map to reduce noise and increase the stability. Then, grids directly ahead of the robot were identified as region of interest (ROI) as shown in Fig. 10(c). Next, peak-to-peak height variation within the ROI was computed, and its normalized value by dividing R was regarded as the $\hat{L}_h$ of the environment at this specific instant. As shown in Fig. 2, if $\hat{L}_h$ lies within the wheeled or legged SOZ, the robot was set to operate in that particular mode. Otherwise, the robot was stopped.

Note that the robot's negotiation of the terrain is a continuous process, and a wide separation of the two half-circular legs is more effective in giving the robot the highest likelihood of successfully navigating the terrain. Therefore, instead of delicately controlling and programming the separation of the two half-circular legs using an analog function of the equivalent step height, a binary decision, wheeled or legged with the longest leg length, was utilized.

IV. EXPERIMENTS AND DISCUSSION

The performances of the proposed strategy were experimentally validated using the *TurboQuad* robot, as shown in Fig. 1. The robot utilizes a central pattern generator as the control architecture, and leg-wheel switching takes about 1–2 strides, as reported in [11]. The color and depth sensors are mounted on the front of the robot. The sensing region of the RGB camera (BIP2-128c, Basler) lies about $200 - 80000$ mm ahead of the robot, with a width of 5000 mm. The update rate for terrain classification is 40 ms. The sensing region of the depth camera (Visionary-T, SICK) is $100 - 4000$ mm ahead of the robot, with a width of 3000 mm. The update rate of the map using the proposed algorithm is about 300 ms

To begin, the performance of the trained network on terrain classification was validated using an independent collected dataset, including 50 random images of each category collected at daytime and nighttime. Statistics from the confusion matrix showed that the overall classification accuracy could reach up to 95% for known categories, as shown in Fig. 9(b). Judging from the results, disturbances including slight motion blur effects, illumination changes, and outliers, such as pedestrians or leaves, could barely influence the accuracy. The output was stable
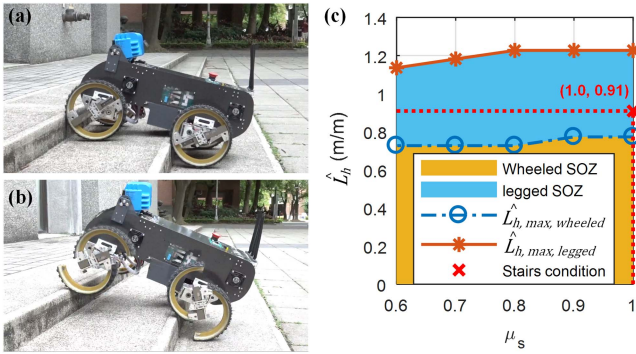
Fig. 11. Robot climbed the stairs using (a) wheeled mode and (b) legged mode. (c) SOZ plot of $v_f = 0.2\ (\mathrm{m/s})$ with the stair condition $\hat{L}_h = 0.91$.

Fig. 12. Average power consumption using only the wheeled mode, only the legged mode, and the proposed strategy.

TABLE I
TRAVERSABILITY SUCCESS RATE COMPARISON

$\hat{L}_h$ (m/m)	Wheel only	Leg only	Proposed strategy	
0.73	5/5	5/5	5/5	
0.86	5/5	5/5	5/5	
0.91	0/5	5/5	5/5	
1.00	0/5	5/5	5/5	
1.18	0/5	5/5	5/5	

enough that further filtering processes were needless. The prediction error mainly came from the testing data with insufficient illumination at night, or the obfuscation over mixed terrains. The worst scenario was when the robot mistakenly identified the uneven terrains as the asphalt or pavement where the robot uses the wheeled mode. Further investigation indicated that this inaccurate classification only happened when the robot approached the stairs or steps from far distances, and the classification was corrected when the target was close enough. Therefore, the model still achieved satisfactory accuracy and stability and evidently worked well on unseen scenarios for known categories.

As an example, Fig. 11 shows the stair-climbing experiment of the robot to exemplify the effectiveness of the SOZ. The stairs have a height of $\hat{L}_h = 0.91$, and the friction coefficient between the robot and stairs (μ_s, μ_k) was assumed to be $(1.0, 0.9)$. The robot with the wheeled mode shown in Fig. 11(a) was not able to climb up the stairs and kept slipping at the corners of the stairs. In contrast, the robot with the legged mode shown in Fig. 11(b) was able to climb up the stairs. The SOZ shown in Fig. 11(c) also indicated that the operating point resided outside the wheeled SOZ and inside the legged SOZ, which matched the robot behavior. The simulation results were therefore verified to capture the motion of the robot in terrain negotiation.

The proposed method was validated in five scenarios: on stairs, steps, and randomly distributed tree root terrain with various $\hat{L}_h$. The $\hat{L}_h$ of the tree root was the height difference between the peak and valley. The robot was set to negotiate the terrain using the wheeled mode, the legged mode, and the proposed strategy. For each mode and terrain, five experimental runs were conducted, and the success rates of terrain negotiation were recorded (Table I). The results verified that the SOZ could act as a critical index for mode selection, and it provided accurate traversability prediction.

Fig. 12 shows the average power consumption of the robot during the trials, which covers the whole obstacle negotiation process, including
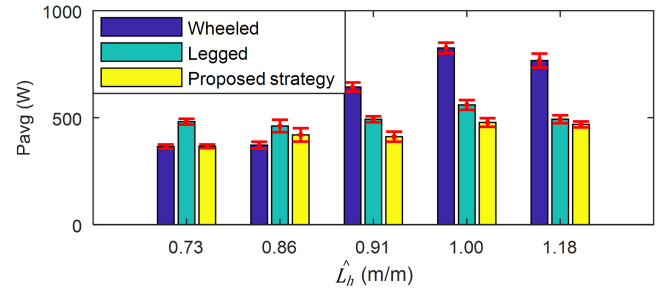
before, during (less than 25% of the time of the experimental run), and after switching. The results indicate that during the wheeled mode, the robot's average power consumption was about 20–30% lower compared to the legged mode when the terrain was negotiable. When the terrain was too high to negotiate, the power increased significantly as the simulation predicted, and the robot in the legged mode had better traversability and better efficiency than the wheeled mode. In short, the proposed strategy, which automatically determined and switched the usage of the wheeled or legged mode, achieved high traversability and lower average power without the need of manual switches. The experimental results show that the traversability success rate and the power consumption of the robot agree with the SOZ suggested from the simulation. Thus, we confirmed that the simplified model in the simulation effectively captured the dynamics of the robot in the real world, and the corresponding optimized selection strategy reached autonomous mode selection with higher energy efficiency.

V. CONCLUSION

This article report on a methodology to develop the behavior decision strategy for the leg-wheel transformable robot *TurboQuad* to autonomously adapt the wheeled mode or legged mode using real-time RGB-Depth information. The concentric dual-leg-wheel model was first developed to evaluate the terrain negotiability of the legged or wheeled mechanism. The results suggested that a single terrain height-related parameter, level height, was sufficient to be utilized and further be concluded as the index, critical operating height, to determine the use of legged or wheeled behavior for empirical implementation.

The two-step motion selection strategy of the robot based on RGB-Depth sensing information was then developed. The first step utilized color information to classify terrain into seven known landscape categories with 95% accuracy, regardless of day or night. For flat terrain such as asphalt or pavement, the wheeled mode was directly utilized. For other terrains, the second step utilized depth information to construct an elevation map for extracting the height variation, so the robot could determine the use of legged or wheeled behaviors in real time using the SOZ. The performance of the strategy was experimentally verified in the robot on five kinds of terrains. The results confirm that the robot using the proposed strategy negotiated the terrain with a 100% success rate and consumed less energy than legged-only mode.

This article the process of investigating the possibility of adding tactile sensing or multiaxis force sensing on the robot, so the physical variation of the terrain such as compliance and damping can be identified by the robot for gait selection.

REFERENCES

[1] S. Seok *et al.*, "Design principles for energy-efficient legged locomotion and implementation on the MIT cheetah robot," *IEEE/ASME Trans. Mechatronics*, vol. 20, no. 3, pp. 1117–1129, Jun. 2015, doi: 10.1109/tmech.2014.2339013.

[2] E. C. Orozco-Madaleno, F. Gomez-Bravo, E. Castillo, and G. Carbone, "Evaluation of locomotion performances for a Mecanum-wheeled hybrid hexapod robot," *IEEE/ASME Trans. Mechatronics*, vol. 26, no. 3, pp. 1657–1667, Jun. 2020.

[3] Z. Wei, G. Song, G. Qiao, Y. Zhang, and H. Sun, "Design and implementation of a leg–wheel robot: Transleg," *ASME J. Mechanisms Robot.*, vol. 9, no. 5, 2017, Art. no. 051001, doi: 10.1115/1.4037018.

[4] T. Okada, W. T. Botelho, and T. Shimizu, "Motion analysis with experimental verification of the hybrid robot PEOPLER-II for reversible switch between walk and roll on demand," *Int. J. Robot. Res.*, vol. 29, no. 9, pp. 1199–1221, 2010, doi: 10.1177/0278364909348762.

[5] K. Tadakuma *et al.*, "Mechanical design of the wheel-leg hybrid mobile robot to realize a large wheel diameter," in *Proc. IEEE/RSJ Int. Conf. Intell. Robots Syst.*, Oct. 2010, pp. 3358–3365, doi: 10.1109/iros.2010.5651912.

[6] Y. S. Kim, G. P. Jung, H. Kim, K. J. Cho, and C. N. Chu, "Wheel transformer: A wheel-leg hybrid robot with passive transformable wheels," *IEEE Trans. Robot.*, vol. 30, no. 6, pp. 1487–1498, Dec. 2014, doi: 10.1109/TRO.2014.2365651.

[7] E. Rohmer, G. Reina, and K. Yoshida, "Dynamic simulation-based action planner for a reconfigurable hybrid leg-wheel planetary exploration rover," *Adv. Robot.*, vol. 24, no. 8-9, pp. 1219–1238, 2010.

[8] C. Zheng and C. Lee, "WheeLeR: Wheel-leg reconfigurable mechanism with passive gears for mobile robot applications," in *Proc. IEEE Int. Conf. Robot. Autom.*, May 2019, pp. 9292–9298, doi: 10.1109/ICRA.2019.8793686.

[9] F. Zhou, X. Xu, H. Xu, Y. Chang, Q. Wang, and J. Chen, "Implementation of a reconfigurable robot to achieve multimodal locomotion based on three rules of configuration," *Robotica*, vol. 38, no. 8, pp. 1478–1494, 2020.

[10] S. C. Chen, K. J. Huang, W. H. Chen, S. Y. Shen, C. H. Li, and P. C. Lin, "Quattroped: A leg-wheel transformable robot," *IEEE/ASME Trans. Mechatronics*, vol. 19, no. 2, pp. 730–742, Apr. 2014, doi: 10.1109/TMECH.2013.2253615.

[11] W. H. Chen, H. S. Lin, Y. M. Lin, and P. C. Lin, "TurboQuad: A novel leg-wheel transformable robot with smooth and fast behavioral transitions," *IEEE Trans. Robot.*, vol. 33, no. 5, pp. 1025–1040, Oct. 2017, doi: 10.1109/tro.2017.2696022.

[12] Y. M. Lin, H. S. Lin, and P. C. Lin, "SLIP-model-based dynamic gait generation in a leg-wheel transformable robot with force control," *IEEE Robot. Autom. Lett.*, vol. 2, no. 2, pp. 804–810, Apr. 2017.

[13] R. J. Full and D. E. Koditschek, "Templates and anchors: Neuromechanical hypotheses of legged locomotion on land," *J. Exp. Biol.*, vol. 202, no. 23, pp. 3325–3332, 1999.

[14] T. Kinugasa and Y. Sugimoto, "Dynamically and biologically inspired legged locomotion: A review," *J. Robot. Mechatronics*, vol. 29, no. 3, pp. 456–470, 2017.

[15] L. Zhornyak and M. R. Emami, "Gait optimization for quadruped rovers," *Robotica*, vol. 38, no. 7, pp. 1263–1287, 2020.

[16] P. Biswal and P. K. Mohanty, "Modeling and effective foot force distribution for the legs of a quadruped robot," *Robotica*, vol. 39, no. 8, pp. 1504–1517, 2021.

[17] F. Aghili, "Quadratically constrained quadratic-programming based control of legged robots subject to nonlinear friction cone and switching constraints," *IEEE/ASME Trans. Mechatronics*, vol. 22, no. 6, pp. 2469–2479, Dec. 2017, doi: 10.1109/TMECH.2017.2755859.

[18] M. Trancossi, "What price of speed? A critical revision through constructal optimization of transport modes," *Int. J. Energy Environ. Eng.*, vol. 7, no. 4, pp. 425–448, 2016, doi: 10.1007/s40095-015-0160-6.

[19] A. Krizhevsky, I. Sutskever, and G. E. Hinton, "ImageNet classification with deep convolutional neural networks," *Commun. ACM*, vol. 60, no. 6, pp. 84–90, 2017, doi: 10.1145/3065386.

[20] I. Dryanovski, W. Morris, and J. Xiao, "Multi-volume occupancy grids: An efficient probabilistic 3D mapping model for micro aerial vehicles," in *Proc. IEEE/RSJ Int. Conf. Intell. Robots Syst.*, 2010, pp. 1553–1559.